

Controlled Redox of Lithium-ion Endohedral Fullerene for Efficient and Stable Metal Electrode-Free Perovskite Solar Cells

Il Jeon,^{*,1,2,‡} Ahmed Shawky,^{1,3,‡} Hao-Sheng Lin,¹ Seungju Seo,¹ Hiroshi Okada,¹ Jin-Wook Lee,^{4,5} Amrita Pal,⁶ Shaun Tan,⁵ Anton Anisimov,⁷ Esko I. Kauppinen,⁸ Yang Yang,⁵ Sergei Manzhos,⁹ Shigeo Maruyama,^{*,1,10} and Yutaka Matsuo^{*,1,11}

¹Department of Mechanical Engineering, The University of Tokyo, 7-3-1 Hongo, Bunkyo-ku, Tokyo 113-8656, Japan

²KU-KIST Green School Graduate School of Energy and Environment, Korea University, 145 Anam-ro, Seongbuk-gu, Seoul 02841, Korea

³Nanomaterials and Nanotechnology Department, Advanced Materials Division, Central Metallurgical R&D Institute (CMRDI), P.O. Box 87 Helwan, Cairo 11421, Egypt

⁴SKKU Advanced Institute of Nanotechnology (SAINT) and Department of Nanoengineering, Sungkyunkwan University, Suwon 16419, South Korea

⁵Department of Materials Science and Engineering and California Nano Systems Institute, University of California, Los Angeles, CA 90095, United States

⁶Department of Mechanical Engineering, National University of Singapore, Block EA #07-08, 9 Engineering Drive 1, Singapore 117576

⁷Canatu, Ltd., Konalankuja 5, FI-00390 Helsinki, Finland

⁸Department of Applied Physics, Aalto University School of Science, P.O. Box 15100, FI-00076 Aalto, Espoo, Finland

⁹Centre Énergie Matériaux Télécommunications, Institut National de la Recherche Scientifique, 1650 boulevard Lionel-Boulet, Varrennes QC J3X1S2, Canada

¹⁰Research Institute for Energy Conservation, National Institute of Advanced Industrial Science and Technology, Tsukuba 305-8565, Japan

¹¹Institute of Materials Innovation, Institutes of Innovation for Future Society, Nagoya University, Furo-cho, Chikusa-ku, Nagoya 464-8603, Japan

KEYWORDS: *Endohedral Fullerene, Metallofullerene, Carbon Nanotube, Perovskite Solar Cells, Stability of Solar Cells*

ABSTRACT: High efficiency perovskite solar cells has underpinned the rapid growth of the field. However, their low device stability limits further advancement. Hygroscopic lithium bis(trifluoromethanesulfonyl)imide (Li^+TFSI^-) and metal electrode are the main causes of the device instability. In this work, the redox reaction between lithium-ion endohedral fullerenes and 2,2',7,7'-tetrakis(*N,N*-di-*p*-methoxyphenylamine)-9,9'-spirobi-fluorene (spiro-MeOTAD) was controlled to optimize the amount of oxidized spiro-MeOTAD and antioxidizing neutral endohedral fullerenes. Application of this mixture to metal-free carbon nanotube (CNT)-laminated perovskite solar cells resulted in 17.2% efficiency with a stability time of more than 1100 hours under severe condition (temperature = 60°C, humidity = 70%). Such high performance is attributed to the uninhibited charge flow, no metal-ion migration, and the enhanced anti-oxidizing activity of the devices.

Perovskite solar cells (PSCs) have become an established photovoltaic technology owing to the exceptional power conversion efficiency (PCE).¹ Despite high PCE, the device stability needs to be substantially improved if PSCs are to be commercialized.² There are two factors responsible for the low stability of PSCs: Li^+TFSI^- and metal electrodes. Use of hygroscopic Li^+TFSI^- in spiro-MeOTAD hole-transporting layer (HTL) results in an uncontrolled oxidation of spiro-MeOTAD as well as moisture-driven degradation.³ In the

same vein, metal electrodes induce a metal ion-migration, which degrades the perovskite material, lowering the device stability.⁴

We previously reported the use of lithium-ion containing [60]fullerene trifluoromethanesulfonylimide salt ($[\text{Li}^+@\text{C}_{60}]\text{TFSI}^-$) instead of Li^+TFSI^- in PSCs.⁵ $[\text{Li}^+@\text{C}_{60}]\text{TFSI}^-$ induced an instant oxidation of spiro-MeOTAD and produced neutral $[\text{Li}^+@\text{C}_{60}]^{\cdot-}$ ($= \text{Li}@\text{C}_{60}$), which functioned as an antioxidant,

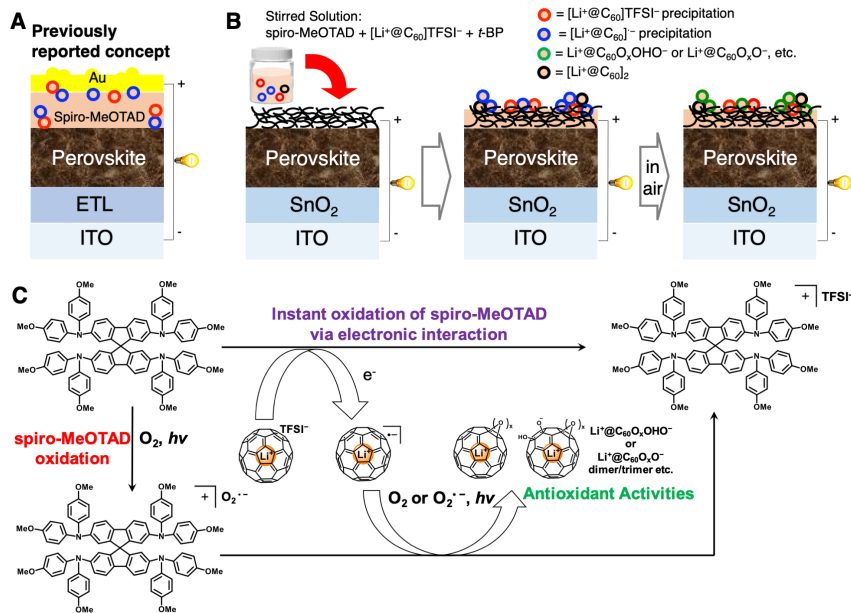


Figure 1. A) Structure of the previously reported device with a metal electrode. B) Proposed structure of this work in which CNTs are used as the top electrode. C) Reaction mechanism of spiro-MeOTAD where $[Li^+@C_{60}]TFSI^-$ is used instead of Li^+TFSI^- .

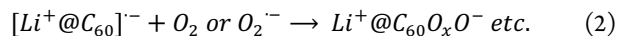
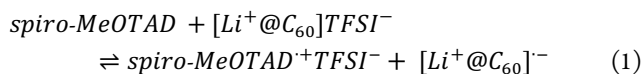
protecting the device from intruding oxygen. With the instant generation of spiro-MeOTAD^{•+}TFSI⁻ and the anti-oxidation activity of $Li^+@C_{60}^-$, the stability of PSCs improved by 10-fold. However, the reported PCEs were relatively low due to the small amount of spiro-MeOTAD^{•+}TFSI⁻ and rough morphology of HTLs, caused by the low solubility of the endohedral fullerene species.⁶ The uncontrolled redox reaction between $[Li^+@C_{60}]TFSI^-$ and spiro-MeOTAD was the root of these problems.

Replacing metal electrodes by carbon conductors has been reported to be one of the most effective ways to improve the PSC stability.⁷ This is because the carbon electrodes prevent metal-ion migration and induce an encapsulation effect.⁸ Among different carbon conductors, aerosol-synthesized free-standing CNTs have shown the highest PCE of 17.6%.^{8,9}

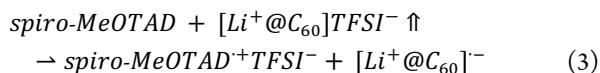
Combining those two technologies and controlling the redox reaction of $[Li^+@C_{60}]TFSI^-$ offer an outstanding synergic solution to the instability and low efficiency of PSCs. Because HTLs are typically spin-coated onto the CNT network in CNT-laminated PSCs,¹⁰ the CNT electrode functioned as a filter when the mixture of spiro-MeOTAD and $[Li^+@C_{60}]TFSI^-$ was applied, causing the undissolved $[Li^+@C_{60}]TFSI^-$ and $Li@C_{60}$ suspensions to stay on top of CNTs. This led to a more effective hole extraction by avoiding $[Li^+@C_{60}]TFSI^-$ aggregations in the charge pathways and an enhanced anti-oxidation activity by exposing $Li@C_{60}$ antioxidants to air. This meant that the reaction time control of the spiro-MeOTAD and $[Li^+@C_{60}]TFSI^-$ solution before the application to the CNT electrode was crucial. We found that a continuous stirring of the solution led to an increase in the spiro-MeOTAD^{•+}TFSI⁻ amount but a decrease in the $Li@C_{60}$ amount. 2 h of stirring time of the mixture gave the best PCE and device stability, as it produced the optimal amount of spiro-MeOTAD^{•+}TFSI⁻ and $Li@C_{60}$, which correspond to an initial PCE and anti-oxidation capability, respectively. A PCE of 17.2% and an operating stability time of 1100 hours under constant illumination in a sever condition (60°C, humidity = 70%) were obtained.

Previously reported endohedral metallofullerene application in PSCs was novel yet presented the limited PCE (Figure 1A).^{5a} This

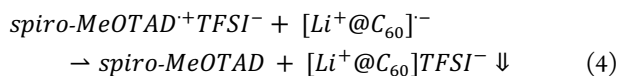
is because the low solubility of $[Li^+@C_{60}]TFSI^-$ and $Li@C_{60}$ led to the formation of aggregations in HTLs. The solubility of $[Li^+@C_{60}]TFSI^-$ in chlorobenzene (CB) is reported to be 5.2 mg ml⁻¹ and 27.5 mg of $[Li^+@C_{60}]TFSI^-$ was dissolved in 1 mL of CB (Figure S1).^{6a} As the separated holes travel through the HTL to the metal electrode, the charge flow was disrupted, resulting in substantially low open-circuit voltage (V_{oc}) and fill factor (FF) of the $[Li^+@C_{60}]TFSI^-$ -based PSCs (Table S1). Application of the spiro-MeOTAD and $[Li^+@C_{60}]TFSI^-$ mixture to the CNT-laminated PSCs filtered out the undissolved $[Li^+@C_{60}]TFSI^-$ and $Li@C_{60}$ aggregations (Figure 1B). Because the separated holes get extracted by CNTs before reaching the aggregations, the CNT-laminated PSC system can give high PCE even at the expense of a PCE loss from the low conductivity of the CNT electrodes.⁹ It was reported that the oxidation of spiro-MeOTAD proceeds according to equation (1) and the anti-oxidation activity follows equation (2) (Figure 1C, Figure S2-S6).^{5a}



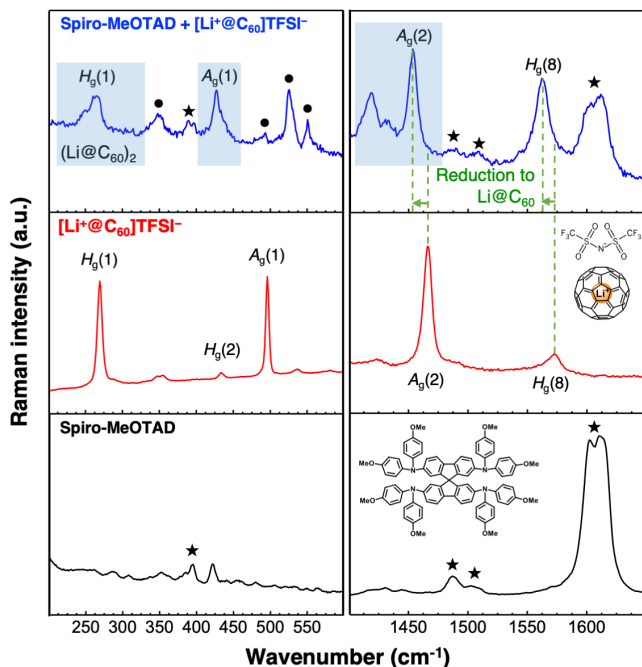
We found that the reaction time between spiro-MeOTAD and $[Li^+@C_{60}]TFSI^-$ is crucial, because not all $[Li^+@C_{60}]TFSI^-$ dissolves in CB. This means that the equilibrium of reaction (1) will depend on the concentration of the reactant $[Li^+@C_{60}]TFSI^-$ and the product $Li@C_{60}$. Since the solubility of $Li@C_{60}$ (<0.1 mg mL⁻¹ in CB, newly found in this work) is even lower than that of $[Li^+@C_{60}]TFSI^-$, the reaction equilibrium will constantly shift to the right, producing spiro-MeOTAD^{•+}TFSI⁻ and $Li@C_{60}$ (3) (Figure S7).



In theory, reaction (3) should cease when most of $[Li^+@C_{60}]TFSI^-$ is dissolved, and reverse the equilibrium like equation (4) (Figure S8).



Scanning electron microscopy (SEM), optical microscopy, and atomic force microscopy (AFM) were used to observe the CNT top electrodes when 0 h-, 2 h-, 5 h-, and 10 h-stirred mixture of spiro-MeOTAD and $[Li^+@C_{60}]TFSI^-$ were applied to the CNTs (Figure 2A – 2D, S9 and S10). Figure 2A shows that the CNT films are intact with the Fe catalysts visible from the magnified inset when the 0 h-stirred solution was applied. The 2 h-stirred solution applied CNT appears to be coated with a thick layer and the catalyst particles are



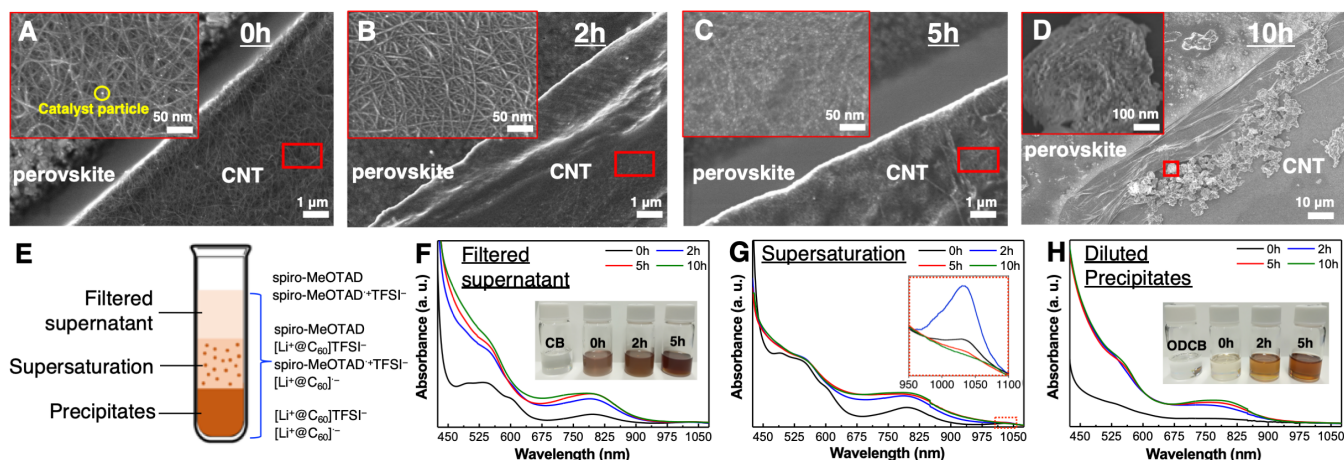
invisible from the magnification (**Figure 2B**). The 5 h-stirred solution-applied CNT appears rough on the surface and the magnification shows less pronounced CNT shapes with newly formed particles (**Figure 2C**). The 10 h-stirred solution-applied CNT films have large aggregations with a size of greater than 300 nm from the inset image (**Figure 2D**). This trend tells us that the reaction between spiro-MeOTAD and $[\text{Li}^+\text{@C}_{60}]\text{TFSI}^-$ leads to a cumulative formation of aggregations over time.

The reaction mixture of spiro-MeOTAD and $[\text{Li}^+\text{@C}_{60}]\text{TFSI}^-$ in three conditions over the reaction time was analyzed (**Figure 2E**). The three conditions were the whole solution (supersaturation), a filtered solution using a 0.2- μm -pore-filter to simulate the CNT (filtered supernatant), and a dilution of the filtered-out residue (diluted precipitates). We used *o*-dichlorobenzene (ODCB) to dilute the residue, because the filtered out aggregation did not dissolve in CB (the solubility of $[\text{Li}^+\text{@C}_{60}]\text{TFSI}^-$ in ODCB is reported to be 15 mg ml⁻¹)^{6a}. Vis-NIR spectroscopy can identify the composition of the HTL solution, specifically, spiro-MeOTAD peak at 390 nm, spiro-MeOTAD⁺TFSI⁻ peak at 500 nm,¹¹ and Li@C_{60} peaks at 800 nm¹² and 1035 nm^{5a,13}. The absorption of the spiro-MeOTAD at 390 nm was too strong in all solutions, indicating that there is an excess amount of spiro-MeOTAD constantly present during the reaction (**Figure 2F–H**). The Vis-NIR spectra of the supernatant solution show that the spiro-MeOTAD⁺TFSI⁻ concentration increases over time (3) (**Figure 2F**). Stirring for 10 h did not decrease the amount of spiro-

MeOTAD⁺TFSI⁻ which means that reaction (4) does occur. The humps at 800 nm indicate oxidized Li@C_{60} according to Campbell and colleagues.^{12a} Yet, our calculation shows that it may also indicate spiro-MeOTAD⁺TFSI⁻ as well (**Figure S11**). This peak gets stronger and blueshifts with the increase in the stirring time, indicating that leaving the reaction for a long time may results in the formation of unwanted Li@C_{60} species despite the air-tight condition of our test. In a separate experiment, leaving Li@C_{60} solution in air blue-shifted the hump at 800 nm, which confirms that Li@C_{60} is oxidized if the mixture is stirred for a long time (**Figure S12**). The antioxidant Li@C_{60} peak did not appear due probably to an insufficient amount of Li@C_{60} after the filtration. The supersaturation showed almost no change in the spiro-MeOTAD⁺TFSI⁻ and the oxidized Li@C_{60} after 2 h (**Figure 2G**). The magnified peaks of Li@C_{60} at 1035 nm showed that the peaks increased in intensity from the 0 h-stirred solution to 2 h-stirred solution, then decreased for the 5 h- and 10 h-stirred solutions (**Figure 2G inset**). This alludes that Li@C_{60} produced in reaction (3) turns into something else when left stirred for more than 2 h. From the diluted precipitates, we could see that the amounts of spiro-MeOTAD⁺TFSI⁻ were small

Figure 3. Raman spectra of spiro-MeOTAD (black), $[\text{Li}^+\text{@C}_{60}]\text{TFSI}^-$ (red), and the mixture of spiro-MeOTAD and $[\text{Li}^+\text{@C}_{60}]\text{TFSI}^-$ (blue) in the low wavenumber region (left) and the high wavenumber region (right).

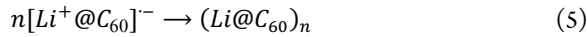
and similar in all samples (**Figure 2H**). Whereas, the hump at 800



nm increased with the stirring time, which indicates an increase in the amount of oxidized $\text{Li}@C_{60}$. There was no neutral $\text{Li}@C_{60}$ peak at 1035 nm, which we ascribe to the ODCB solvent.¹⁴ Additional experiments using XPS (Figure S13 and S14), ¹⁹F nuclear magnetic resonance (NMR) (Figure S15), and dynamic light scattering measurement (Figure S16) corroborate the reaction mechanism as well, which are discussed in detail in the supporting information.

Raman spectroscopy was used to identify the generated $\text{Li}@C_{60}$ species. **Figure 3** shows the Raman spectra of spiro-MeOTAD (black), $[\text{Li}^+@C_{60}]\text{TFSI}^-$ (red),¹⁵ and the 5 h-stirred mixture of both (blue) in the low and high wavenumbers (**Figure S17**). The $A_g(2)$ and $H_g(8)$ modes of the $[\text{Li}^+@C_{60}]\text{TFSI}^-$ spectrum shifted to lower wavenumbers in the mixture. This confirms the reduction to $\text{Li}@C_{60}$ (indicated by green).¹⁶ The spiro-MeOTAD peaks still remain after the reaction (closed star). The positions of the $H_g(1)$ and $A_g(2)$ and the downshift of the $A_g(1)$ indicate the formation of $(\text{Li}@C_{60})_2$, arising from the reduced symmetry of the covalently bonded C_{60} .^{12a} The increasing intensity of the peak at 1419 cm^{-1} is typical of fullerene dimerization (**Figure S18 and S19**).¹⁷ The splitting of $H_g(1)$ and $A_g(1)$ ¹⁸ indicates a possible polymerization of fullerene.¹⁹ The new peaks near the $H_g(1)$ and $A_g(1)$ (closed circles) probably come from the mixing of vibrational modes caused by symmetry perturbation. This reveals that $\text{Li}@C_{60}$ undergoes further reaction not only with oxygen (2) but with other $\text{Li}@C_{60}$ to form dimers and polymers (5) (**Figure S20**).

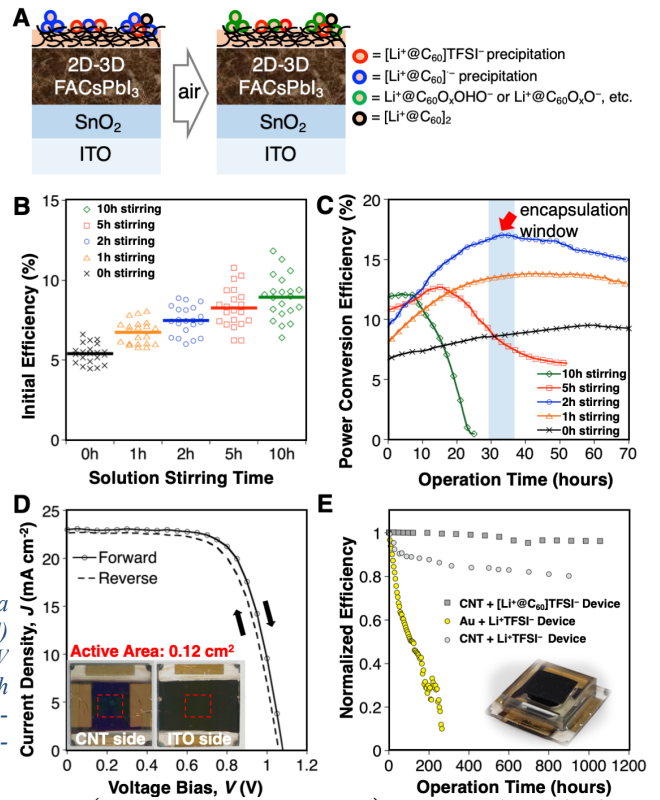
Figure 4. A) Illustration of the endohedral fullerene species on a CNT-laminated PSC when left in air. B) The initial PCEs and C) PCE changes of the $[\text{Li}^+@C_{60}]\text{TFSI}^-$ -applied CNT-PSCs. D) $J-V$ curves of the champion 2 h-stirred HTL-applied CNT-PSC with pictures of the device as an inset. E) Normalized PCE of the encapsulated PSCs tested in this work with the picture of the encapsulated $[\text{Li}^+@C_{60}]\text{TFSI}^-$ -applied CNT-PSC.



PSCs were fabricated in a structural configuration of glass/indium tin oxide (ITO)/ SnO_2 /[(phenethylamine (PEA))₂PbI₄]₁[(formamidinium (FA))_{0.97}Cs_{0.03}PbI₃]₅₉ (2D-3D FACsPbI₃)/CNT, onto which the mixture of spiro-MeOTAD and $[\text{Li}^+@C_{60}]\text{TFSI}^-$ was applied (**Figure 4A**).^{9c,20} It is worth noting that 4-tert-butylpyridine (*t*-BP) was necessary for PSCs to work and there was no reaction between $[\text{Li}^+@C_{60}]\text{TFSI}^-$ and *t*-BP (**Table S2 and Figure S21**). The initial PCEs of the $[\text{Li}^+@C_{60}]\text{TFSI}^-$ -applied CNT-laminated PSCs showed that the photovoltaic performance increased with the increase in the stirring time of the HTL (**Figure 4B and S22, Table 1 and S3**). We surmise that the initial PCE is proportional to the amount of spiro-MeOTAD⁺TFSI⁻. It should be mentioned that the reproducibility of the initial PCEs of PSCs were relatively low for the long hour-stirred HTL solutions. This is due to the reaction rate being dependent on the stirring condition, such as temperature and stirring speed. Continuous

illumination on the PSCs in air improved the performance of the devices for a certain period of time then decreased slowly (**Figure 4C and S23**).^{5a} The maximum PCEs, the time taken before

reaching the maximum PCE, and the PCE attenuation rates all depended on the HTL reaction time (**Figure S24**). This is also supported by our oxygen transmittance rate (OTR), in which the change of OTR values follow the predicted degrees of antioxidation activity (**Figure S25**). The 2 h-stirred HTL-applied CNT-PSCs exhibited the highest PCE of 17.2% with a slow PCE attenuation rate, which implies the optimal balance of spiro-MeOTAD⁺TFSI⁻ and



$\text{Li}@C_{60}$ (**Figure 4D and S26, Table 1**). By encapsulating the device at the right timing, the long-term stability time of more than 1100 h stability under constant illumination in a severe condition (60°C, 70% humidity) was recorded (**Figure 4e and S27**). The data reveals that the $[\text{Li}^+@C_{60}]\text{TFSI}^-$ -used CNT-laminated PSCs show by far greater device stability than those of the metal electrode-based PSCs (**Table S4**) and the Li^+TFSI^- -used CNT-laminated PSCs.

In summary, we fabricated metal electrode-free CNT-PSCs with the mixture of spiro-MeOTAD and $[\text{Li}^+@C_{60}]\text{TFSI}^-$. The CNT electrode functioned as a natural filter for the endohedral metallofullerene aggregations. This prevented the aggregations from interfering the charge flow, enhancing PCE of the PSCs greatly. It was found that the redox time control of spiro-MeOTAD and $[\text{Li}^+@C_{60}]\text{TFSI}^-$ was crucial in obtaining high PCE and high stability. We found that a continuous reaction generated $\text{Li}@C_{60}$ aggregations, losing their antioxidation capacity. Thus, 2 h of reaction time was optimal which gave the maximum photovoltaic performance in terms of efficiency and stability. With the new reaction mechanism

Table 1. Photovoltaic parameters of the CNT-laminated PSCs to which spiro-MeOTAD with different dopants were applied.

Dopant	Reaction time	J_{sc} (mA cm^{-2})	V_{oc} (V)	FF	Initial PCE (%)	PCE (%)
Li^+TFSI^-	N/A	23.0	1.08	0.68	0	16.9
	0 h	16.4	0.86	0.68	6.8	9.51
$[\text{Li}^+@C_{60}]\text{TFSI}^-$	1 h	21.8	0.94	0.67	7.9	13.8
	2 h	23.1	1.09	0.67	9.3	17.2
	5 h	21.0	0.97	0.62	10.8	12.7
	10 h	21.9	1.05	0.52	11.9	12.1

found, this work demonstrates metal electrode-free PSCs with unprecedentedly high stability, thanks to no ion-migration and the enhanced antioxidant activity of $\text{Li}@C_{60}$.

ASSOCIATED CONTENT

Supporting Information

The Supporting Information is available free of charge on the ACS Publications website.

The Supporting Information includes experimental details, morphology investigation, computational study, reaction mechanism, Vis-NIR spectroscopy, XPS analysis, ^{19}F NMR analysis, dynamic light scattering measurement, Raman spectroscopy, and device performance tests.

AUTHOR INFORMATION

Corresponding Author

*E-mail: il.jeon@spc.oxon.org (I.J.), maruyama@photon.t.u-tokyo.ac.jp (S.M.) and matsuo@photon.t.u-tokyo.ac.jp (Y.M.)

Notes

Authors declare no competing financial interests.

ACKNOWLEDGMENT

We thank Dr. Hiroshi Ueno (Tohoku University), Dr. Yasuhiko Kasama, and Kazuhiko Kawachi (Idea International Inc.) for involvement through scientific discussion. ‡These authors contributed equally. We gratefully acknowledge the Research and Education Consortium for Innovation of Advanced Integrated Science by Japan Science and Technology (JST) and Japan Society for the Promotion of Science JSPS KAKENHI Grant Numbers JP15H05760, JP17K04970, JP17F17364, JP18H05329, and JP19K15669. I.J. thanks Yashima Environment Technology Foundation for financial support.

REFERENCES

- (1) (a) Lee, M. M.; Teuscher, J.; Miyasaka, T.; Murakami, T. N.; Snaith, H. J. Efficient hybrid solar cells based on meso-superstructured organometal halide perovskites. *Science* **2012**, *338* (6107), 643. (b) Green, M. A.; Ho-Baillie, A.; Snaith, H. J. The emergence of perovskite solar cells. *Nat. Photonics* **2014**, *8* (7), 506. (c) Seok, S. I.; Grätzel, M.; Park, N.-G. Methodologies toward highly efficient perovskite solar cells. *Small* **2018**, *14* (20), 1704177. (d) Leijtens, T.; Bush, K. A.; Prasanna, R.; McGehee, M. D. Opportunities and challenges for tandem solar cells using metal halide perovskite semiconductors. *Nat. Energy* **2018**, *3* (10), 828. (e) NREL efficiency chart <https://www.nrel.gov/pv/device-performance.html>. (f) Li, X.; Ibrahim Dar, M.; Yi, C.; Luo, J.; Tschumi, M.; Zakeeruddin, S. M.; Nazeeruddin, M. K.; Han, H.; Grätzel, M. Improved performance and stability of perovskite solar cells by crystal crosslinking with alkylphosphonic acid ω -ammonium chlorides. *Nat. Chem.* **2015**, *7* (9), 703.
- (2) (a) Domanski, K.; Alharbi, E. A.; Hagfeldt, A.; Grätzel, M.; Tress, W. Systematic investigation of the impact of operation conditions on the degradation behaviour of perovskite solar cells. *Nat. Energy* **2018**, *3* (1), 61. (b) Yue, Y.; Salim, N.; Wu, Y.; Yang, X.; Islam, A.; Chen, W.; Liu, J.; Bi, E.; Xie, F.; Cai, M.; Han, L. Enhanced stability of perovskite solar cells through corrosion-free pyridine derivatives in hole-transporting materials. *Adv. Mater.* **2016**, *28* (48), 10738. (c) Quan, L. N.; Yuan, M.; Comin, R.; Voznyy, O.; Beauregard, E. M.; Hoogland, S.; Buin, A.; Kirmani, A. R.; Zhao, K.; Amassian, A.; Kim, D. H.; Sargent, E. H. Ligand-stabilized reduced-dimensionality perovskites. *J. Am. Chem. Soc.* **2016**, *138* (8), 2649. (d) Park, N.-G.; Grätzel, M.; Miyasaka, T.; Zhu, K.; Emery, K. Towards stable and commercially available perovskite solar cells. *Nat. Energy* **2016**, *1* (11), 16152.
- (3) (a) Liu, J.; Wu, Y.; Qin, C.; Yang, X.; Yasuda, T.; Islam, A.; Zhang, K.; Peng, W.; Chen, W.; Han, L. A dopant-free hole-transporting material for efficient and stable perovskite solar cells. *Energy Environ. Sci.* **2014**, *7* (9), 2963. (b) Cappel, U. B.; Daeneke, T.; Bach, U. Oxygen-induced doping of spiro-MeOTAD in solid-state dye-sensitized solar cells and its impact on device performance. *Nano Lett.* **2012**, *12* (9), 4925. (c) Bryant, D.; Aristidou, N.; Pont, S.; Sanchez-Molina, I.; Chotchunangachaval, T.; Wheeler, S.; Durrant, J. R.; Haque, S. A. Light and oxygen induced degradation limits the operational stability of methylammonium lead triiodide perovskite solar cells. *Energy Environ. Sci.* **2016**, *9* (5), 1655. (d) Seo, J.-Y.; Kim, H.-S.; Akin, S.; Stojanovic, M.; Simon, E.; Fleischer, M.; Hagfeldt, A.; Zakeeruddin, S. M.; Grätzel, M. Novel p-dopant toward highly efficient and stable perovskite solar cells. *Energy Environ. Sci.* **2018**, *11* (10), 2985. (e) Jeon, N. J.; Na, H.; Jung, E. H.; Yang, T.-Y.; Lee, Y. G.; Kim, G.; Shin, H.-W.; Seok, S. I.; Lee, J.; Seo, J. A fluorene-terminated hole-transporting material for highly efficient and stable perovskite solar cells. *Nat. Energy* **2018**, *3* (8), 682. (f) Lim, K.-G.; Ahn, S.; Kim, Y.-H.; Qi, Y.; Lee, T.-W. Universal energy level tailoring of self-organized hole extraction layers in organic solar cells and organic-inorganic hybrid perovskite solar cells. *Energy Environ. Sci.* **2016**, *9* (3), 932.
- (4) Domanski, K.; Correa-Baena, J.-P.; Mine, N.; Nazeeruddin, M. K.; Abate, A.; Saliba, M.; Tress, W.; Hagfeldt, A.; Grätzel, M. Not all that glitters is gold: metal-migration-induced degradation in perovskite solar cells. *ACS Nano* **2016**, *10* (6), 6306.
- (5) (a) Jeon, I.; Ueno, H.; Seo, S.; Aitola, K.; Nishikubo, R.; Saeki, A.; Okada, H.; Boschloo, G.; Maruyama, S.; Matsuo, Y. Lithium-ion endohedral fullerene ($\text{Li}^+@C_{60}$) dopants in stable perovskite solar cells induce instant doping and anti-oxidation. *Angew. Chemie Int. Ed.* **2018**, *57* (17), 4607. (b) Aoyagi, S.; Nishibori, E.; Sawa, H.; Sugimoto, K.; Takata, M.; Miyata, Y.; Kitaura, R.; Shinohara, H.; Okada, H.; Sakai, T.; Ono, Y.; Kawachi, K.; Yokoo, K.; Ono, S.; Omote, K.; Kasama, Y.; Ishikawa, S.; Komuro, T.; Tobita, H. A layered ionic crystal of polar $\text{Li}@C_{60}$ superatoms. *Nat. Chem.* **2010**, *2* (8), 678.
- (6) (a) Okada, H.; Matsuo, Y. Anion exchange of $\text{Li}^+@C_{60}$ salt for improved solubility. *Fuller. Nanotub. Car. N.* **2014**, *22* (1–3), 262. (b) Matsuo, Y.; Okada, H.; Ueno, H. *Endohedral Lithium-containing Fullerenes*; Springer Singapore: Singapore, **2017**.
- (7) (a) Mei, A.; Li, X.; Liu, L.; Ku, Z.; Rong, Y.; Xu, M.; Hu, M.; Chen, J.; Yang, Y.; Grätzel, M.; Han, H. A hole-conductor-free, fully printable mesoscopic perovskite solar cell with high stability. *Science* **2014**, *345* (6194), 295. (b) Jeon, I.; Seo, S.; Sato, Y.; Delacou, C.; Anisimov, A.; Suenaga, K.; Kauppinen, E. I.; Maruyama, S.; Matsuo, Y. Perovskite solar cells using carbon nanotubes both as cathode and as anode. *J. Phys. Chem. C* **2017**, *121* (46), 25743.
- (8) (a) Aitola, K.; Domanski, K.; Correa-Baena, J.-P.; Sveinbjörnsson, K.; Saliba, M.; Abate, A.; Grätzel, M.; Kauppinen, E.; Johansson, E. M. J.; Tress, W.; Hagfeldt, A.; Boschloo, G. High temperature-stable perovskite solar cell based on low-cost carbon nanotube hole contact. *Adv. Mater.* **2017**, *29* (17), 1606398. (b) Ahn, N.; Jeon, I.; Yoon, J.; Kauppinen, E. I.; Matsuo, Y.; Maruyama, S.; Choi, M. Carbon-sandwiched perovskite solar cell. *J. Mater. Chem. A* **2018**, *6* (4), 1382.
- (9) (a) Jeon, I.; Matsuo, Y.; Maruyama, S. Single-walled carbon nanotubes in solar cells. *Top. Curr. Chem.* **2018**, *376* (1), 4. (b) Jeon, I.; Xiang, R.; Shauky, A.; Matsuo, Y.; Maruyama, S. Single-walled carbon nanotubes in emerging solar cells: synthesis and electrode applications. *Adv. Energy Mater.* **2019**, *9* (23), 1801312. (c) Lee, J.-W.; Jeon, I.; Lin, H.-S.; Seo, S.; Han, T.-H.; Anisimov, A.; Kauppinen, E. I.; Matsuo, Y.; Maruyama, S.; Yang, Y. Vapor-assisted ex-situ doping of carbon nanotube toward efficient and stable perovskite solar cells. *Nano Lett.* **2019**, *19* (4), 2223.
- (10) Aitola, K.; Sveinbjörnsson, K.; Correa-Baena, J.-P.; Kaskela, A.; Abate, A.; Tian, Y.; Johansson, E. M. J.; Grätzel, M.; Kauppinen, E. I.; Hagfeldt, A.; Boschloo, G. Carbon nanotube-based hybrid hole-transporting material and selective contact for high efficiency perovskite solar cells. *Energy Environ. Sci.* **2016**, *9* (2), 461.
- (11) Nguyen, W. H.; Bailie, C. D.; Unger, E. L.; McGehee, M. D. Enhancing the hole-conductivity of spiro-OMeTAD without oxygen or lithium salts by using spiro(TFSI)₂ in perovskite and dye-sensitized solar cells. *J. Am. Chem. Soc.* **2014**, *136* (31), 10996.
- (12) (a) Gromov, A.; Krawez, N.; Lassesson, A.; Ostrovskii, D. I.; Campbell, E. E. B. Optical properties of endohedral $\text{Li}@C_{60}$. *Curr. Appl. Phys.* **2002**, *2* (1), 51. (b) Supur, M.; Kawashima, Y.; Larsen, K. R.; Ohkubo, K.; Jeppesen, J. O.; Fukuzumi, S. Robust inclusion complexes of crown ether fused tetrathiafulvalenes with $\text{Li}^+@C_{60}$ to afford efficient photodriven charge separation. *Chem. A Eur. J.* **2014**, *20* (43), 13976.
- (13) Ueno, H.; Aoyagi, S.; Yamazaki, Y.; Ohkubo, K.; Ikuma, N.; Okada, H.; Kato, T.; Matsuo, Y.; Fukuzumi, S.; Kokubo, K. Electrochemical reduction of cationic $\text{Li}^+@C_{60}$ to neutral $\text{Li}^+@C_{60}^-$: isolation and characterisation of

- endohedral [60] fulleride. *Chem. Sci.* **2016**, 7 (9), 5770.
- (14) Supur, M.; Kawashima, Y.; Ohkubo, K.; Sakai, H.; Hasobe, T.; Fukuzumi, S. Graphene oxide–Li⁺@C₆₀ donor–acceptor composites for photoenergy conversion. *Phys. Chem. Chem. Phys.* **2015**, 17 (24), 15732.
- (15) Gromov, A.; Ostrovskii, D.; Lassesson, A.; Jönsson, M.; Campbell, E. E. B. Fourier transform infrared and raman spectroscopic study of chromatographically isolated Li@C₆₀ and Li@C₇₀. *J. Phys. Chem. B* **2003**, 107 (41), 11290.
- (16) (a) Kuzmany, H.; Pfeiffer, R.; Hulman, M.; Kramberger, C. Raman spectroscopy of fullerenes and fullerene-nanotube composites. *Philos. Trans. R. Soc. London. Ser. A Math. Phys. Eng. Sci.* **2004**, 362 (1824), 2375. (b) Kuzmany, H.; Matus, M.; Burger, B.; Winter, J. Raman scattering in C₆₀ fullerenes and fullerides. *Adv. Mater.* **1994**, 6 (10), 731. (c) Kosaka, M.; Tanigaki, K.; Prassides, K.; Margadonna, S.; Lappas, A.; Brown, C. M.; Fitch, A. N. Superconductivity in Li_xCsC₆₀ fullerides. *Phys. Rev. B* **1999**, 59 (10), R6628. (d) Sathish, M.; Miyazawa, K.; Sasaki, T. Nanoporous fullerene nanowhiskers. *Chem. Mater.* **2007**, 19 (10), 2398.
- (17) (a) Kuzmany, H.; Plank, W.; Winter, J.; Dubay, O.; Tagmatarchis, N.; Prassides, K. Raman spectrum and stability of (C₅₉N)₂. *Phys. Rev. B* **1999**, 60 (2), 1005. (b) Plank, W.; Pichler, T.; Kuzmany, H.; Dubay, O.; Tagmatarchis, N.; Prassides, K. Resonance Raman excitation and electronic structure of the single bonded dimers (C₆₀)₂ and (C₅₉N)₂. *Eur. Phys. J. B* **2000**, 17 (1), 33.
- (18) Akasaka, T., Nagase, S. (Eds.), *Endofullerenes: Developments in Fullerene Science*. Vol. 3. Springer Netherlands, Dordrecht, **2002**.
- (19) (a) Rao, A. M.; Zhou, P.; Wang, K.-A.; Hager, G. T.; Holden, J. M.; Wang, Y.; Lee, W.-T.; Bi, X.-X.; Eklund, P. C.; Cornett, D. S.; Duncan, M. A.; Amster, I. J. Photoinduced polymerization of solid C₆₀ films. *Science* **1993**, 259 (5097), 955. (b) Lavrentiev, V.; Vacik, J.; Naramoto, H.; Narumi, K. Polymerization of solid C₆₀ under C₆₀⁺ cluster ion bombardment. *Appl. Phys. A* **2009**, 95 (3), 867.
- (20) Thote, A.; Jeon, I.; Lee, J.-W.; Seo, S.; Lin, H.-S.; Yang, Y.; Daiguji, H.; Maruyama, S.; Matsuo, Y. Stable and reproducible 2D/3D formamidinium–lead–iodide perovskite solar cells. *ACS Appl. Energy Mater.* **2019**, 2 (4), 2486.

Insert Table of Contents artwork here

